MDPI

Article

A Partial Eruption of a Sigmoid Filament in the Small Dipole Active Region 12734

Jihong Liu [1,2], Yin Zhang [3], Yuhong Zheng [4], Yu Liu [2]* and Jie Chen [3]

1 School of Science, Shijiazhuang University, Shijiazhuang 050035, China; 1102066@sjzc.edu.cn
2 School of Physical Science and Technology, Southwest Jiaotong University, Chengdu 610031, China
3 National Astronomical Observatories, Chinese Academy of Sciences, Beijing 100012, China; zhangyin@bao.ac.cn (Y.Z.); chenjie@bao.ac.cn (J.C.)
4 Shijiazhuang Post and Telecommunications Technical College, Shijiazhuang 050011, China; zhengyh@sjzpc.edu.cn
* Correspondence: lyu@swjtu.edu.cn

Abstract: We present a detailed analysis of a partial eruption of a sigmoid filament lying along the polarity inversion line (PIL) of the small active region (AR) NOAA 12734 (with an area of 1.44×10^3 square megameters). The active filament was rooted in a dipole sunspot of the AR. The eruption was associated with a C1.3 flare and subsequent large-scale coronal disturbances. During its solar disk passage before the flare, the AR had the following characteristics: (1) Most of the time, the magnetic field lines in the AR showed a sigmoidal structure ('L1') in the low corona and arc-shaped loops (i.e., 'L2') in the upper atmosphere. (2) An 'X'-shaped structure was formed between the original 'S'-shaped magnetic loop ('L1') and the newly rising one ('L3') between the main positive and negative magnetic polarities of the sunspots, and the intersection point of flux ropes 'L1' and 'L3' corresponds well with the area where the initial extreme-ultraviolet (EUV) 1600 Å brightening of the flare occurred. (3) The AR disobeyed the hemispherical helicity rule and had magnetic twist and writhe of the same signs, i.e., its magnetic helicity/current helicity were positive in the northern hemisphere. (4) Sustained magnetic emergence and cancellation occurred before the flare. Therefore, the magnetic reconnection of highly twisted helical flux ropes under the confinement of the overlying magnetic fields is probably responsible for the partial eruption of the filament.

Keywords: flares; filaments/prominences; magnetic fields; reconnection

1. Introduction

Small active regions (ARs) with certain magnetic field characteristics can produce flares and further trigger relatively large disturbances. These small ARs have relatively simple structures that enable us to capture clearer physical images of them. Since the launch of the Solar Dynamics Observatory (SDO) [1], the high temporal and high spatial resolution multiwavelength observations taken by the Atmospheric Imaging Assembly (AIA) [2] on board the SDO have provided us with an unprecedented opportunity not only to directly image major events but also to study rather weak ARs with very modest flares. Such events tend to occur near regions of cancelling photospheric magnetic fields and are thought to be directly associated with magnetic field reconnection.

The magnetic flux rope (MFR) is a fundamental structure in solar eruptions ([3,4], and references therein). Flux ropes could become unstable in the case of magnetic emergence or cancellation in the magnetic topological structure. Consequently, magnetic reconnection takes place and free energy is released, thus forming a solar flare [5–9]. For decades, a lot of research on the magnetic reconnection model, which explains the exact trigger of the eruption, has been conducted [10–17], which includes the tether-cutting reconnection [18] and the breakout reconnection [19,20]. However, it is recognized that the magnetic breakout is a universal model for solar eruptions [16]. Liu et al. (2021) [20] suggested that 'collisional

shearing', i.e., bipole–bipole interaction during the flux emergence, is a common process in driving the major activities in emerging ARs. Yang et al. (2019) [3] reported a confined flare captured by the AIA/SDO and considered that the external reconnection between the rising highly twisted flux rope and a part of the overlying potential field lines plays an important role in the confined flare formation. Ruan et al. (2015) [13] investigated the penumbrae decay and the correlated decline of the photospheric transverse field component, and they considered that the preflare magnetic structure from the photosphere to the corona becomes more vertical with time. Xu et al. (2020) [14] studied a failed eruption from a helical kink-unstable prominence and gave evidence for the existence of a helical magnetic structure showing the twist converting to writhe.

Filament eruptions can be full, failed, or partial. In partial eruptions, filaments usually split into two parts, with one part being fully erupted and the other remaining [21]. Sigmoids are S-shaped structures that emit soft X-rays and extreme ultraviolet (EUV). They are always described either by flux ropes or by highly sheared magnetic arcades since their central parts are approximately aligned with the photospheric PIL [22]. Sigmoidal regions are significantly more likely to be eruptive than nonsigmoidal regions [5]. It is appealing to associate sigmoids with kinked flux ropes [23], although it remains controversial whether the observed sigmoids carry sufficient magnetic twist for the onset of the kink instability [24–26].

Kink instability is the process whereby magnetic twist (the winding of magnetic field lines around an axis) in a confined flux system is abruptly converted to magnetic writhe (the winding or deforming of the axis itself) [24]. In a cylindrical flux rope of radius r and length L, the safety factor $q = \frac{rB_{z(r)}}{LB_{\theta(r)}}$, which is related to the twist angle through $\Phi = \frac{2\pi}{q}$, is key to flux-rope stability ([5] and the references). External kink instability occurs when q < 1. However, the real threshold of twist for instability lies at 2.5 π according to analytical and numerical studies [17]. However, it is debatable whether helical kink instability plays a significant role in triggering eruptions for the MFR-hosted filament, which is widely believed to be a dense and cool plasma material that is hosted by an MFR or sheared magnetic field [27]. Zhang et al. [17] presented an example of filament formation via the tether-cutting reconnection of two nearby filaments and considered that helical kink instability may be the trigger of the filament eruption. Jing et al. [28] studied 38 solar flares (stronger than M5) and found that the unsigned twist number appears to play little role in discriminating between confined and ejective events. Régnier et al. [25] studied the 3D coronal magnetic field of AR 8151 using the nonlinear force-free hypothesis and concluded that the eruptive phenomenon occurring in this AR is likely due to the kink instability in the highly twisted flux tube and not in the less twisted S-shaped flux tube. Wang et al. (2017) [29] studied the background field of 60 two-ribbon flares of M-and-above classes and found that the decay index increases monotonously with increasing height for most of the flares.

It has been revealed statistically that the preferred chirality of solar magnetic fields for ARs is primarily negative in the northern hemisphere and positive in the southern, which is called the hemispherical helicity rule (HH rule) [30–34]. ARs disobeying the HH rule have strong current helicity, so they are usually more eruptive than those obeying the rule.

In this study, we report the observations of a partial eruption of a sigmoid filament associated with a C1.3 flare that erupted in the small area AR NOAA 12734 that disobeys the HH rule. Our main aim is to investigate the dynamic evolution of the AR and discuss the role of the AR on the mechanism of the partial filament eruption and the following confinement. This paper is arranged as follows: The data and methods are described in Section 2. The results of the magnetic topological structure and chirality of the AR are described in Section 3. Conclusions and discussions are presented in Section 4.

2. Data and Methods

The AR NOAA 12734 appeared on the solar disk during the time period from 4 to 11 March 2019. A C1.3-class solar flare occurred in this AR on 8 March, followed immedi-

ately by large-scale coronal disturbances. These disturbances included two EUV waves [35], one bidirectional quasiperiodic fast-propagating (QFP) magnetosonic wave [36], and one fast coronal mass ejection (CME). The integrated soft X-ray flux over the range of 1–8 Å was recorded by the Geostationary Operational Environmental Satellite (GOES). According to the GOES record, the flare started at 03:07 UT. It reached the first peak at 03:18 UT and the second peak at 03:36 UT. It ended at 04:00 UT. Around the first flaring peak, the EUV wave was excited, and after the second flaring peak, the two QFP waves began to propagate in opposite directions. These activities were recorded by the SDO/AIA. After checking all AIA wavelengths, the 1600, 171, 131, and 304 Å wavelengths were selected to present the dynamic evolution of these activities in the present work. At about 05:54 UT, a CME on the northwest side of the sun was observed by the Large Angle and Spectrometer Coronagraph (LASCO) C2. The moving brightening front of the CME reached the height of about $3.8R_{\odot}$.

Space-Weather Active Region Patches (SHARPs) are a vector magnetic field data product which are recorded by the Helioseismic and Magnetic Imager (HMI) onboard the SDO, with a temporal resolution of 720 s [37–40]. The 180° azimuth ambiguity is resolved, and the helioprojective image is remapped onto a cylindrical equal area projection, where each pixel has the same surface (about 0.5″ at disk center) [39,40].

Based on this time series data set, the velocity perpendicular to magnetic field lines (even the vector velocity) in the photosphere can be derived using the differential affine velocity estimator for vector magnetograms (DAVE4VM [41]) method. The relative helicity flux (helicity flux hereafter) across a surface can be computed with the following equation [42,43],

$$\frac{dH_m}{dt} = -2 \oint_S (\mathbf{A}_p \cdot \mathbf{V}_t) B_n ds + 2 \oint_S (\mathbf{A}_p \cdot \mathbf{B}_t) V_n ds, \tag{1}$$

where $\mathbf{A}_p$ is the vector potential [44] of the potential field $\mathbf{B}_p$; $\mathbf{B}_t$ and $\mathbf{B}_n$ denote the tangential and normal magnetic fields; and $\mathbf{V}_t$ and $\mathbf{V}_n$ are the tangential and normal components of horizontal velocity $\mathbf{V}$, the velocity perpendicular to magnetic field lines. $\mathbf{V}$ can be produced with the DAVE4VM method. $\mathbf{A}_p$ can be calculated conveniently based on the observed light-of-sight (LOS) magnetic field. Furthermore, the helicity accumulation ΔH is the time integration of the measured helicity flux dH/dt [43,45]. AR 12734 is a newly emerging flux region, with magnetic observation covering almost the entire appearance of the AR. Its helicity was computed by integrating over time the helicity flux during the entire emergence of the AR, i.e., from 08:24 UT on 4 March to 16:00 UT on 11 March. To reduce the noise effects, the velocity in regions with low flux density, less than 10 Mx cm^{-2} (Gauss), is set to zero when computing the dH/dt. If adopting a higher threshold, such as 100 Mx cm^{-2}, roughly 1σ of field measurement, the resulting ΔH will become 14% smaller, with a very similar evolution curve.

It is usually believed that the helicity of a flux tube can be decomposed into twist and writhe. We calculate the parameter α_{av}, which is usually used as a measure of magnetic twist per unit length [46,47]. It is described as follows:

$$\alpha_{av} = \frac{\sum B_z J_z}{\sum B_z^2}, \tag{2}$$

where $\mathbf{B}_z$ is the vertical component of the magnetic field, and $\mathbf{J}_z$ is the vertical current density [39,40]. We also calculate the proxy of writhe by dividing the tilt angle by the separation between the centroid of two polarities:

$$Writhe = -Tilt/d, \tag{3}$$

where the '*Tilt*' is the angle between the line connecting the centroid of opposite polarities and the local parallel of latitude passing through the centroid of the leading polarity [48]. Furthermore, 'd' is the separation between the centroid of two polarities [49]. We set tilt angles as being positive when they are measured in the counterclockwise direction

and are in the interval from $-90°$ to $90°$ [34]. Only pixels with a field strength greater than 300 Mx cm^{-2}, roughly 3σ of field measurement, are included for the computation of α_{av} [40].

3. Results

The overview of AR 12734 is shown in Figure 1. The images were taken at around 03:05 UT on 8 March, immediately before the start of the C1.3 flare. The leading and trailing sunspots have negative and positive polarities (panel (b)), respectively. The letters 'P1', 'P2', and 'P3' mark the main positive polarities, and 'N1', 'N2', and 'N3' mark the negative ones. In the 304 Å image (panel (c)), the filament shows obvious sigmoidal morphology, which is marked with a green letter 'S' and is visible in the 171 Å image. In the 171 Å image (panel (d)), there were lots of large-scale loops connecting the AR's positive and negative polarities. In particular, there were three typical kinds of loops (denoted by the green arrow and letters 'L1', 'L2', 'L3'). L1 connects N1 and P1. It is sigmoidal and corresponds spatially to the sigmoidal filament in the chromosphere. L2 connects N1 and P3. Morphologically, it looks like a quasipotential flux tube. L3 connects N1 and P1 along a straight line in the top view. It is wide and partly brightened. Later analysis will show that L1 and L3 (tracked by cross symbols in the small 171 image) are different magnetic field line clusters of the same flux tube, which is highly twisted.

3.1. The Magnetic Topological Structure of the AR

3.1.1. The Sigmoidal Structure and the Eruptive Events

The time evolution of the AR from the AIA 171 Å and 131 Å images is shown in Figure 2. The visible transverse sigmoidal structure forms before 00:00 UT, as shown in Figure 1c,d. It finally evolves as the helical postflare loop, as shown in Figure 2d. The main sunspot is negative and marked 'N1' in Figure 1b. It is connected to all of the three positive polarities of the AR. The magnetic loop L1 and L3 cross each other near the top of N2 and form an 'X'-shaped structure. Both above and below the intersection of the 'X'-shape, funnel-shaped magnetic field line structures are formed, as mentioned by Miao et al. (2021) in their Figure 1 [50]. This provides the necessary magnetic topological condition for the explosion wave event.

After the initiation of the C1.3 flare, the magnetic loop 'L2' begins to rise. The part adjacent to the outer edge of 'Lf1' erupts successfully, and the magnetic line of force nearby gradually opens (see Animation 1 for details). At the same time, the first large-angle/circular EUV wave occurs (see Animation 2 for details). However, some parts of the magnetic loop 'L1' fail to erupt and fall back, as shown in Figure 2b,f and marked with 'Lf1'. Right after the fall of the 'Lf1' material, the flare reaches the second X-ray radiation peak and is accompanied by the bidirectional QFP wave. Meanwhile, the first signs of posteruption arcade (PEA) are already evident in Figure 2b,f.

Meanwhile, the magnetic structure marked with 'Lf2' in Figure 2c,g rises and erupts (see Animation 1 for details); subsequently, the second EUV wave is generated on the solar surface (see Animation 2 for details). 'Lf2' does not reach the outer space, which may imply the confinement of the overlying magnetic field. Lf2 is at the periphery of the AR and represents horizontal loops that are likely to be a part of the overlying fields. Although no decay index was calculated for that location due to observation limitations, one can still expect the presence of strong overlying fields. Being obstructed by the overlying magnetic arc, 'Lf2' changes its propagation direction and moves along the magnetic field line. Meanwhile, the magnetic field lines in the left part of the AR gradually open to form a coronal dimming. The peripheral magnetic field lines on the top of 'Lf2' open gradually. We can see that lines of force in the regions marked 'R1' and 'R2' in Figure 2b,f rotate clockwise obviously. On the other hand, at the beginning of the flare, the coronal dimming is in the southeast and northwest above the AR, as shown in Figure 2a. After the explosion, the coronal dimming is in the northeast and southwest above the AR, as shown in Figure 2d. This fact implies that the magnetic loop of the AR was untwisted after the explosion.

'Se' in Figure 2d marks the newly formed S-shaped filament channel about 4 h after the eruptive events. From Figure 2h, we can also see a newly formed similar S-shaped filament corresponding to the 'Se'. The writhe (twisting along the axial direction) of the filament has become obviously smaller than that of the sigmoidal filament before the eruption. Above the partially relaxed filament, the PEA evolves into a postflare loop.
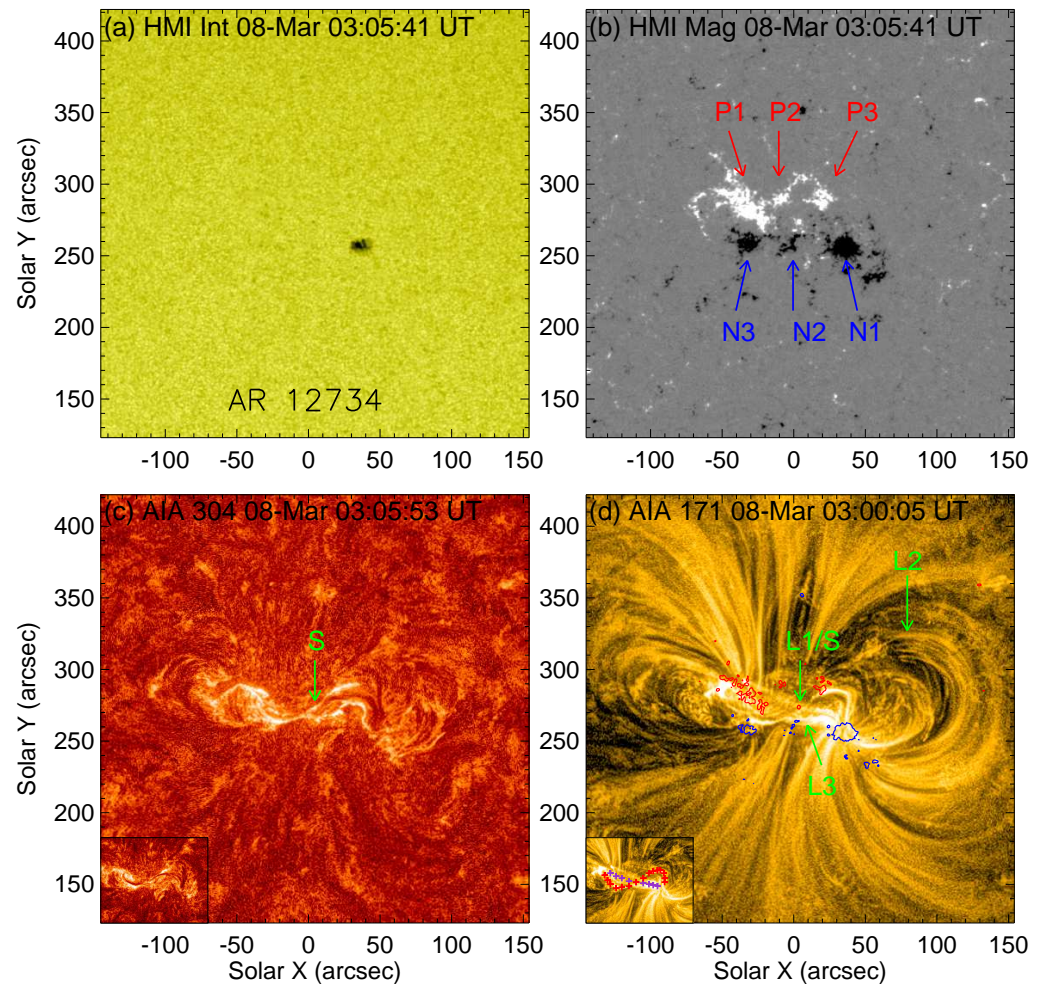
Figure 1. Overview of AR 12734 at 03:00−03:05 UT, right before the GOES flare started. (**a**,**b**) HMI intensity gram and light-of-sight (LOS) magnetogram, respectively. (**c**,**d**) AIA 304 and 171 Å images, respectively. The red letters 'P1', 'P2', and 'P3' mark the main positive polarities, and the blue letters 'N1', 'N2', and 'N3' mark the negative ones. The green letters 'L1', 'L2', and 'L3' in panel (**d**) mark the magnetic loops between 'N1' and 'P1' (along the sigmoidal structure), 'N1' and 'P3', and 'N1' and 'P1' (along a straight line), separately. The red/blue contours in panel (**d**) mark the LOS field of 320 Gauss. A small 304/171 image is placed at the bottom-left corner in panels (**c**)/(**d**), with the field of view (FOV) as 150″ × 120″. The well-sigmoid-shaped filament in the small 304 image was taken at 03:00 UT, and the red/purple crosses in the small 171 image mark the loop 'L1'/'L3'.
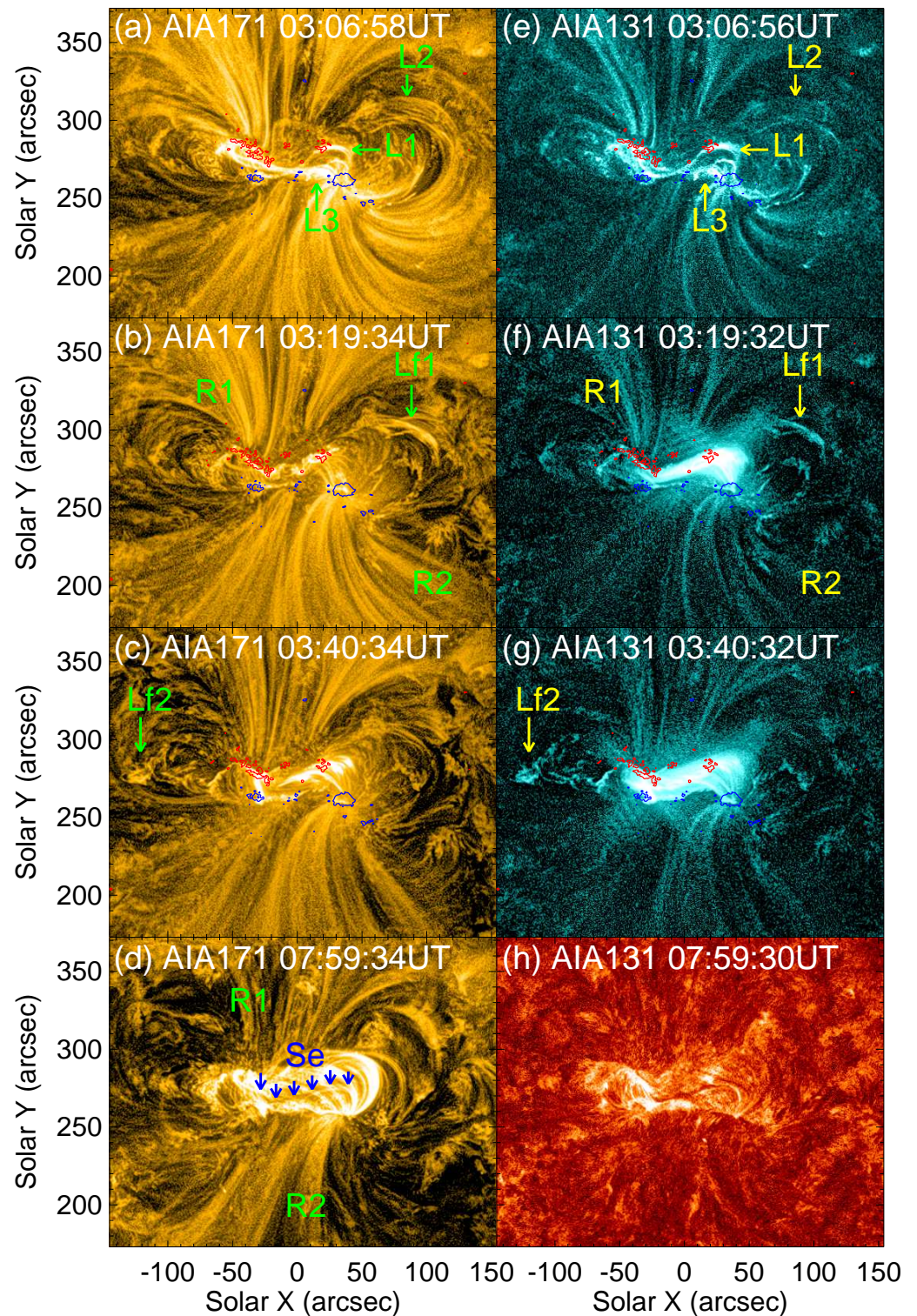
Figure 2. The temporal evolution of AR 12734 as shown in the AIA 171 Å and 131 Å images taken on 8 March 2019. The red/blue contours mark the LOS field of 320 Gauss. The green/yellow letters 'L1', 'L2', and 'L3' in panels (**a**)/(**e**) mark the magnetic loops similar to Figure 1. 'Lf1'/'Lf2' in panels (**b**,**f**)/(**c**,**g**) mark the backflows of the partially erupted internal filament. Lf1 and Lf2 occurred 1 and 4 min after the two flaring peaks, separately. 'Se' in panel (**d**) marks the newly formed S-shaped filament channel about 4 h after the eruptive events. A similar sigmoidal filament can be seen in the AIA 304 Å image shown in panel (**h**). It is less twisted than before. 'R1' and 'R2' in panels (**b**,**d**) mark the region where the line of force rotates clockwise.

3.1.2. The 'X'-Shaped Structure of Sunspot Pairs

Figure 3 presents the vector magnetic field and the calculated velocity distribution of the AR by using the SHARPs data from the SDO/HMI. The yellow contours mark the FPIL [17]. The PIL is severely twisted and resembles two 'S' shapes connected together. Its middle part is an Ω shape. This is a very explosive magnetic field morphology.
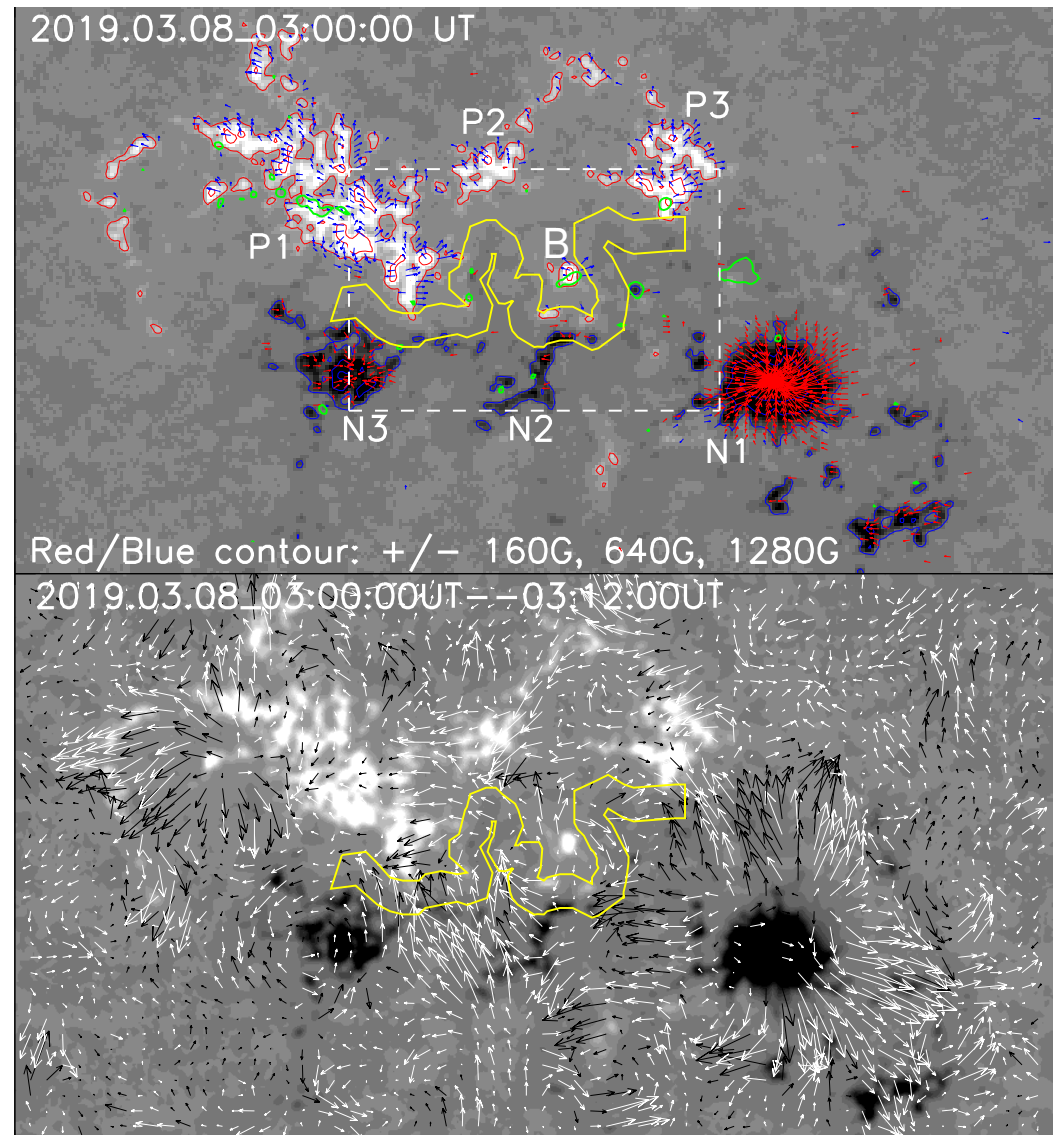
Figure 3. Top: The vector magnetic field of AR 12734. The blue and red arrows indicate the positive and negative transverse magnetic fields, respectively. The yellow solid contours mark the flaring polarity inversion line (FPIL). The green contours outline the area where the initial EUV 1600 Å brightening occurred for the flare. **Bottom**: The velocity distribution calculated using DAVE4VM overlaid on the grayscale map of the LOS magnetic field distribution. The FOV is $171'' \times 98''$.

NOAA 12734 is a newly emerging AR and a β region following Hale's law for Solar Cycle 24. As an AR in the northern hemisphere, its leading polarity is negative. We can see from Figure 3 that the connecting lines of the sunspot pairs present an 'X'-shaped structure: P1−N1 and P3/P2−N2/N3. The corresponding above- and low-lying magnetic loop structures can be seen from Figures 1d and 2a.

The white letter 'N1' in the top panel of Figure 3 marks the main negative polarity. It can also be seen from Figure 3 that the horizontal magnetic field of 'N1' shows a slight clockwise rotation, which means a right-handed twist of the field lines about its axis

within the flux tube. More obvious right-hand-spiral magnetic field lines around 'N1' can be seen in Figures 1d and 2a,e. Hale [51] first reported the magnetic twist structure on the sun, pointing out that about 80% of the magnetic fiber structures of sunspots rotate counterclockwise in the northern hemisphere and clockwise in the southern hemisphere. AR 12734 does not follow the statistical law of the rotation direction, and this abnormal characteristic may play an important role for its relatively strong activity. The velocity distribution right before the C1.3 flare calculated using the DAVE4VM method is shown in the bottom panel of Figure 3. The main negative sunspot has a continuous outward flow and shows a slight counterclockwise rotation movement, which may be caused by a clockwise spiral. This is in agreement with Figure 1 in Démoulin et al. (2003). When a flux tube rises through the photosphere, the point where the tube crosses the photosphere moves with velocity $\mathbf{U}_f$, which points in the opposite direction to $\mathbf{B}_t$ (tangential components of the magnetic field) [43]. On the other hand, it can be seen from Figure 4 that there is sustained magnetic convergence and cancellation along the PIL (see Animation 3 for details). The white rectangles in Figure 4 mark the areas with obvious magnetic emergence before the flare. Furthermore, on the lower-left and upper-right sides of the white rectangles along the PIL, apparent magnetic cancellation appears, as indicated by the green arrows in Figure 4. Such magnetic emergence and cancellation may lead to the magnetic reconnection and further trigger the partial eruption of the filament.
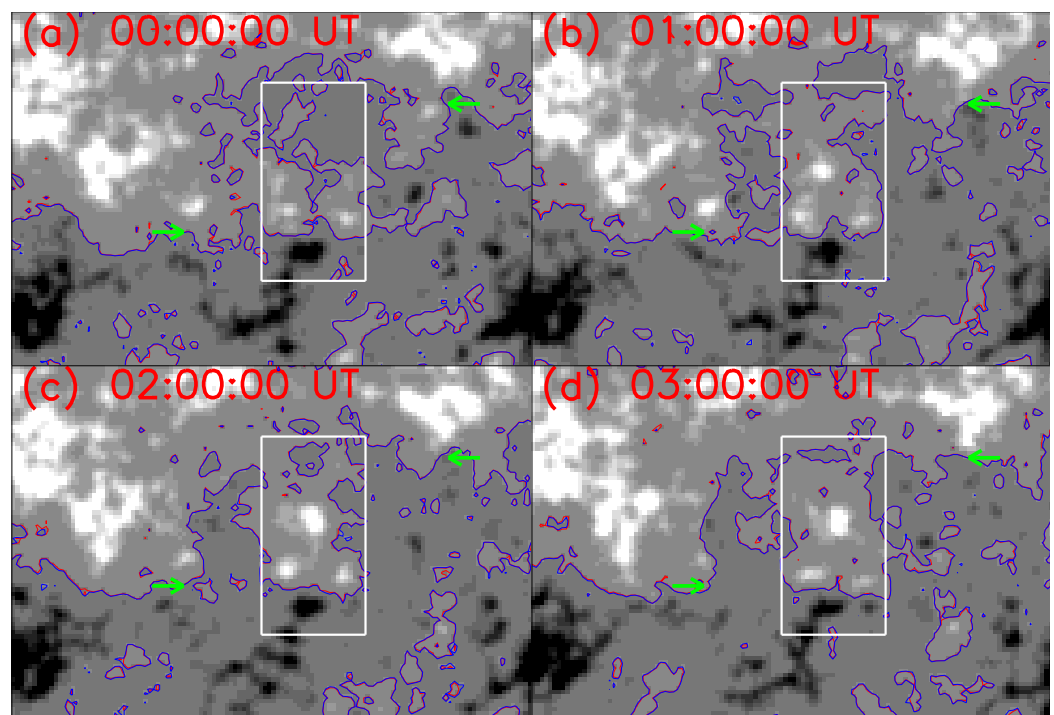
Figure 4. The dynamic evolution of the LOS magnetic field of AR 12734 in the core region, which is indicated by the dashed white box in Figure 3, top panel. The FOV is $61'' \times 41''$. The red/blue contours mark the LOS field of 1 Gauss and can represent the PIL. The white rectangles mark the areas with obvious magnetic emergence before the flare. Furthermore, apparent magnetic cancellation appears on both sides of the rectangles along the PIL, as indicated by the green arrows.

3.2. The Magnetic Chirality of the AR

3.2.1. Magnetic Helicity Flux and Helicity Accumulations

Both surface motion and magnetic emerging flux can transport magnetic twist through the photosphere and then accumulate the magnetic helicity in the corona. Meanwhile, significant twisted features are observed in this case; therefore, kink instability may be the possible trigger for the eruptive event. To quantitatively investigate the helicity, we calculate the helicity accumulation ΔH and the average alpha density α_{av}.

Figure 5 shows the average alpha density, unsigned flux, writhe, and helicity accumulation as a function of time for AR 12734. Note that the abrupt change of writhe is due to its definition range from $-90°$ to $90°$. The dashed line marks the first GOES flare maximum, at 03:18 UT on 8 March 2019. The second flare maximum occurred 18 min later. All of the events, including the flare, filament eruption, and EUV waves, occurred and finished within 30 min. As a result, the accumulated helicity was about 2.2×10^{41} Mx^2 (Figure 5) around 03:07 UT on 8 March when the C1.3 flare initiated. It was far smaller than the amount needed for a CME-associated major flare, which is usually around several times 10^{43} Mx^2 [52]. A necessary condition for the occurrence of an X-flare is that the peak helicity flux has a magnitude greater than 2×10^{40} Mx^2 h^{-1} [53]. For AR 12734, the calculated maximum helicity flux was about 10^{39} Mx^2 h^{-1} around the flare time. However, considering the fact that the magnetic flux of the AR was less than 10^{22} Mx, the helicity accumulation per unit flux was relatively large. In fact, the ratio of helicity accumulation to the square of magnetic flux reached $\Delta H/F^2 = 0.23$. This ratio is a dimensionless quantity and represents the turns of flux rope [54]. An X-class flare with a ratio index of 0.04 is reported [54]. The larger ratio index of 0.23 for AR 12734 implies that the AR has a right-handed spiral, which is likely strong enough to cause an explosion.
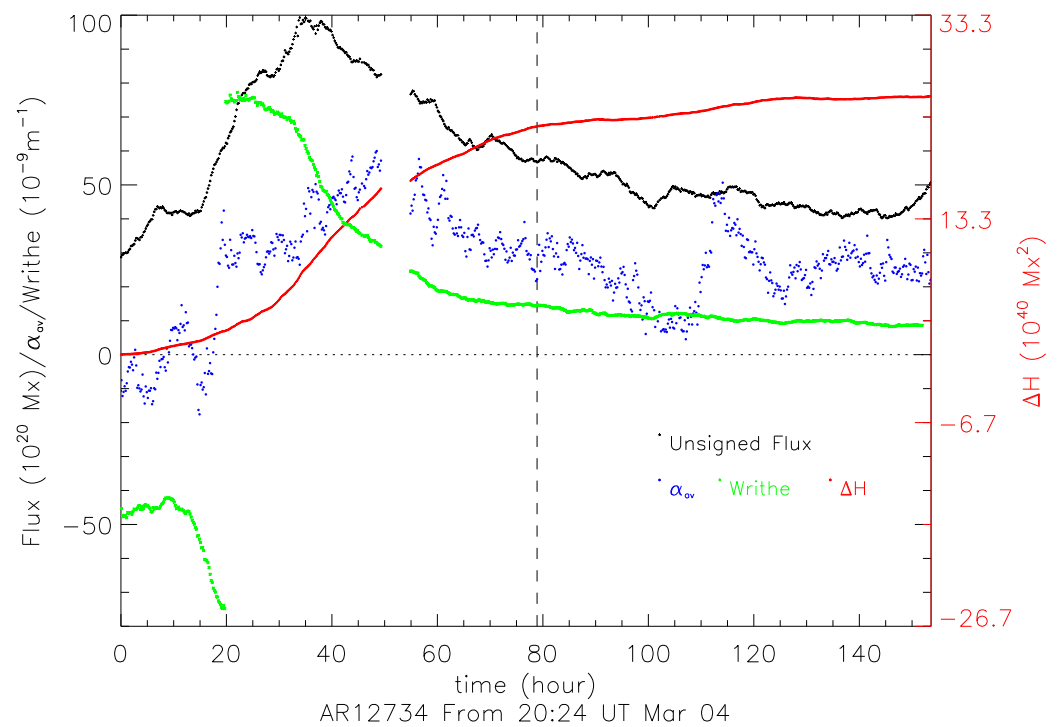
Figure 5. The average alpha density, unsigned flux, writhe, and helicity accumulation as a function of time for AR 12734. The dashed line marks the first GOES flare maximum.

3.2.2. Right-Handed Spiral: Positive Magnetic Twist and Writhe of the AR

From Figure 5, we can see further that the helicity accumulation, α_{av}, and writhe are all displayed with positive signs. Note that AR 12734 is located in the northern hemisphere. Therefore, the studied AR has a magnetic twist and writhe of the same signs and disobeys the HH rule. This supports the viewpoint that the hemispherical preference is more obvious for ARs with magnetic twist and writhe of opposite signs than for ARs with the same signs [40,48]. The positive signs of twist and writhe are consistent with the sigmoidal magnetic loop in Figures 1 and 2 and with the clockwise rotation of the sunspot umbra fibrils shown in Figure 3. Undoubtedly, the magnetic field in the AR is right-handed.

AR 12734 is a newly emerging flux region. When the AR emerged from the photosphere, the unsigned flux and mean alpha density had increased for more than two days,

then decreased. The writhe and helicity accumulation kept increasing. Their growth slowed down before the flare/filament eruption and remained almost constant after the event. ΔH is the helicity transported to the corona, and α_{av} is that which remains in the photosphere. When a flux tube rises through the convection zone, it can be deformed by Coriolis force or convective turbulence. Furthermore, this deformation produces magnetic writhe and an equivalent twist of the opposite sign in the tube to conserve helicity [40,43]. In this scenario, one can expect that the sign of the acquired writhe of an AR will be opposite to that of its twist. On the other hand, if a flux tube initially has a twist great enough to lead to kink instability, part of the twist is converted to writhe. In this case, the signs of the twist and writhe are the same [40]. The chirality of the studied AR follows the latter scenario. AR 12734 possibly obtains its right-handed twist deep down through a dynamo process which generates a twist that is not (or is weakly) linked to the *tilt*/writhe [48]. Zhang et al. (2010) [47] studied AR vector magnetograms for more than 20 years at observatories in Mees, Huairou, and Mitaka and found areas of the 'wrong' sign at the ends of the butterfly wings as well as at their very beginnings. Liu et al. (2014b) [49] studied 82 bipolar ARs and found that bipolar ARs having the same signs of twist and writhe do not have a strong hemispheric preference, which may suggest that the twist generated by the dynamo process has no hemispheric preference. The fact that AR 12734 appears at the end of Solar Cycle 24 and that it has the same signs of twist and writhe (both positive) may be reasons that it disobeys the HH rule. This may be due to the phase relation between the toroidal and poloidal fields generated by Babcock–Leighton-type dynamo models [55].

Until one day before the C1.3 flare, the α_{av} kept increasing while the writhe kept decreasing. This probably implies that the writhe kept converting to twist in a confined flux system. On the other hand, for the newly emerging flux region, there will naturally be a decrease/increase in writhe/α_{av} in the initial flux emerging stage [56]. It needs further analysis to determine which one plays the most important role.

3.2.3. The Partial Eruption and Kink Instability

The nonlinear force-free magnetic field (NLFFF) extrapolation from the photospheric vector magnetograms is a general method used to reconstruct the coronal field. By using the high spatial and temporal resolution observing data provided by the SDO/ SHARPs, we extrapolate the coronal magnetic structures using NLFFF modeling [57], before which the photospheric magnetogram is preprocessed to best suit the force-free conditions [58]. The calculation is performed within a cubic box of 340 × 192 × 192 uniform grid points with $\Delta x = \Delta y = \Delta z = 0.5''$.

Figure 6 shows the extrapolation field 7 min before the flare initiation. It well matches the magnetic loops observed between the main negative polarities and each positive polarity shown in Figure 2. The field lines of the low-lying magnetic flux ropes L1 and L3 present the twisted magnetic morphology of the AR. L1 and L3 are different magnetic field line clusters of the same flux tube. Furthermore, L2 represents the large-scale overlying confinement field. The white letter 'C' marks the intersection point of L1 and L3 where the filament is lifted and can be used as the lower limit of the apex height. It has a good spatial correspondence with one of the green contours in Figure 3, which outlines the initial EUV 1600 Å brightening of the flare (marked with the white letter 'B' in Figure 3). Considering the continuous magnetic emergence and cancellation along the PIL, we propose that the magnetic reconnection of highly twisted helical flux ropes is probably responsible for the eruption of the filament. Due to the confinement of the overlying field (L2), the sigmoid filament can only partially erupt, resulting in the observed evolution of the event.

When the twist of the flux rope exceeds a threshold, a kink instability occurs. The decay index is an important factor in deciding whether a kink instability can eventually develop a successful eruption [59]. The decay index can be calculated by $n = (-z/B)\partial B/\partial z$, where B is the magnetic field strength and z is the height above the solar surface [60–62]. By using potential field extrapolation with vector magnetic field data taken at 03:00 UT, we investigate the decay index on the FPIL, i.e., the intersection of the PIL and the flare region

at the peak time of AIA 1600 Å. The yellow solid contours in the top panel of Figure 3 mark the FPIL of the AR. The PIL is identified from a longitudinal magnetic field map and dilated with a circular kernel (radius r = 1.9 Mm). From the extrapolated magnetic field, the height of the sheared arcade, where the filament is lifted (marked 'C' in Figure 6), is about 27.2 Mm. Meanwhile, the decay index n is about 1.74 at the height of 27.2 Mm, which is larger than the common threshold value 1.1 ± 0.1 for the eruptive filament [60]. This is consistent with the initiation of the eruption of the sigmoidal filament. However, part of the filaments erupt successfully while the other part of them (Lf1 and Lf2) fail to erupt in the studied case. They are located on the periphery of the AR and represent horizontal loops that are likely to be a part of the overlying fields. Although the decay index of the large-scale overlying magnetic field cannot be accurately calculated due to observation limitations, the fact that Lf1 and Lf2 did not reach the outer space may imply the confinement of the strong overlying magnetic field.
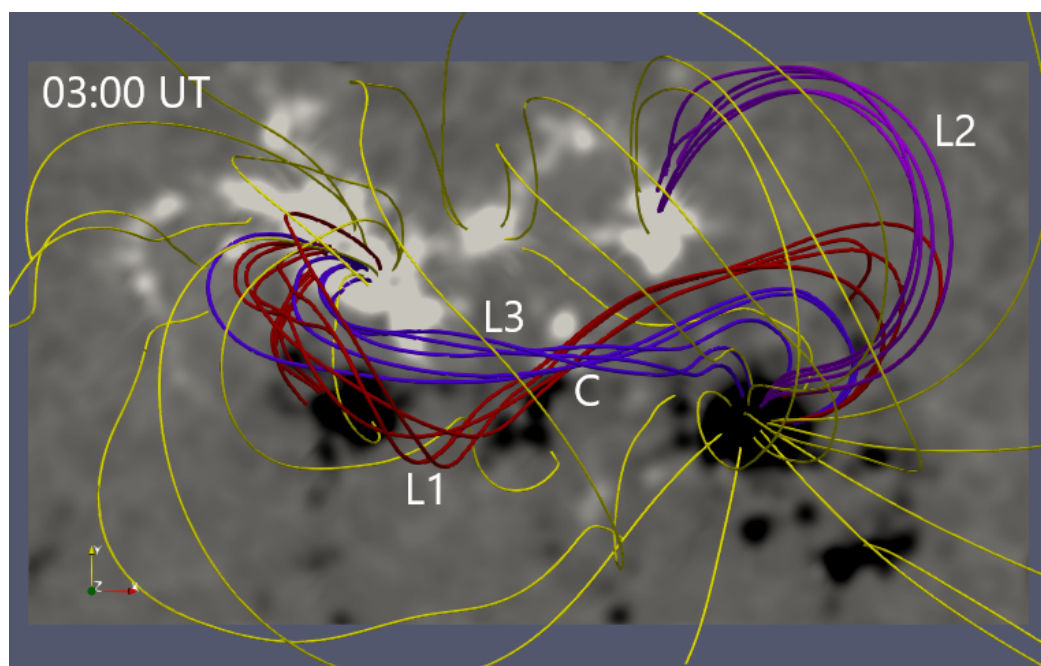
Figure 6. NLFFF extrapolation from 8 March 2019 at 03:00 UT (7 min before the flare initiation). The red, purple, blue lines outline the low-lying magnetic flux ropes cospatial with 'L1', 'L2', and 'L3' marked in Figures 1d and 2a. The yellow lines mark the large-scale overlying loops. The white letter 'C' marks the intersection point of 'L1' and 'L3' where the filament is lifted.

4. Conclusions and Discussions

In this study, based on the high-resolution multiwavelength observations from the SDO, we present an investigation of a partial eruption of a sigmoid filament on 8 March 2019 in the AR NOAA 12734, which was associated with a C1.3 flare and large-scale coronal disturbances.

Our main results and conclusions are summarized as follows:

1. The AR shows a sigmoidal structure in the low corona. It disobeys the hemispherical helicity rule and has magnetic twist and writhe of the same signs. These properties make it eruptive.

2. An 'X'-shaped structure is formed between the original 'S'-shaped magnetic loop and the newly rising one between the main positive and negative magnetic polarities of sunspots. The intersection point of magnetic flux ropes L1 and L3 correspond well with the initial brightening of the flare. Therefore, the continuous magnetic emergence and cancellation along the PIL may cause the magnetic reconnection of the highly

twisted helical flux ropes, which is probably responsible for the observed evolution of the event.

3. The calculated maximum helicity flux is about 10^{39} Mx^2 h^{-1} around the flare time. The ratio of helicity accumulation to the square of magnetic flux reaches $\Delta H/F^2 = 0.23$ for AR 12734. The AR has a right-handed spiral which is likely strong enough to cause a flare.

4. The decay index n is about 1.74 at the height of 27.2 Mm, which is more than enough to support a partial filament eruption.

In the absence of side-view observation, no significant apex rotation is observed during the whole observational phase for the partial filament eruption associated with the flare. Thus, we are not sure whether the kink instability could be the possible trigger for this event. However, before the flare, the PIL of the AR is severely twisted and looks like an Ω-shape. It is a significantly twisted feature. Meanwhile, the α_{av}/writhe of the AR keep increasing/decreasing before the flare, which implies the conversion from the writhe to twist before the eruption. Furthermore, the two parameters tend to stabilize after the flare. After the explosion, the direction of the coronal dimming above the AR has a significant clockwise rotation, and the newly formed S-shaped structure after the flare become less twisted than the sigmoidal filament before the flare. These imply that the magnetic loop of the AR was untwisted after the explosion. The decay index n of the studied AR is larger than the common threshold value for a successfully erupted filament. Therefore, we propose that the partial eruption of the filament and the following large-scale disturbance occurring in this AR are probably due to the kink instability in the highly twisted flux tube.

In this study, we present a thorough analysis of a rather weak AR with a partial eruption filament associated with a very modest flare. This unusual data selection makes the work exclusive and useful because the majority of flare investigations consider strong flare events. This research demonstrates a conceptual idea that flares on the sun are self-similar phenomena following common laws. In this case, the sustained emergence and cancellation make the magnetic reconnection of L1 and L3 on the 'X' point happen and trigger the partial eruption of the filament of the ARs associated with the C1.3 flare, accompanied by the opening and relaxation of the nearby magnetic line of force and clockwise rotation of the main spot. The raised MFR pushes the large-scale overlying confinement field outward, simultaneously transporting helicity and energy to the upper atmosphere and subsequently resulting in the global EUV waves and CME.

References

1. Pesnell, W.D.; Thompson, B.J.; Chamberlin, P.C. The Solar Dynamics Observatory (SDO). *Sol. Phys.* **2012**, *275*, 3−15. [CrossRef]
2. Lemen, J.R.; Title, A.M.; Akin, D.J.; Boerner, P.F.; Chou, C.; Drake, J.F.; Duncan, D.W.; Edwards, C.G.; Friedlaender, F.M.; Heyman, G.F.; et al. The Atmospheric Imaging Assembly (AIA) on the Solar Dynamics Observatory (SDO). *Sol. Phys.* **2012**, *275*, 17−40. [CrossRef]
3. Yang, S.H.; Zhang J.; Song, Q.; Bi, Y.; Li, T. Two-step Evolution of a Rising Flux Rope Resulting in a Confined Solar Flare. *Astrophys. J.* **2019**, *878*, 38. [CrossRef]
4. Zhang, Yin.; Liu, J.; Tan, B.; Zhu, X.; Yan, Y. Dynamic Evolution of Magnetic Flux Ropes in Active Region 11429. I. EUV Observations. *Astrophys. J.* **2022**, *940*, 125. [CrossRef]
5. Liu, R. Magnetic flux ropes in the solar corona: Structure and evolution toward eruption. *Res. Astron. Astrophys.* **2020**, *20*, 165. [CrossRef]
6. Shibata, K.; Masuda, S.; Shimojo, M.; Hara, H.; Yokoyama, T.; Tsuneta, S.; Kosugi, T.; Ogawara, Y. Hot-Plasma Ejections Associated with Compact-Loop Solar Flares. *Astrophys. J.* **1995**, *451*, L83. [CrossRef]
7. Lin, J.; Forbes, T.G. Effects of reconnection on the coronal mass ejection process. *J. Geophys. Res.* **2000**, *105*, 2375. [CrossRef]
8. Zweibel, E.G.; Yamada, M. Magnetic Reconnection in Astrophysical and Laboratory Plasmas. *Annu. Rev. Astron. Astrophys.* **2009**, *47*, 291−332. [CrossRef]
9. Deng, Y.Y.; Wang, J.X.; Yan, Y.H.; Zhang, J. Evolution of Magnetic Nonpotentiality in NOAA AR 9077. *Sol. Phys.* **2001**, *204*, 11−26. [CrossRef]
10. Su, J.; Jing, J.; Wang, S.; Wiegelmann, T.; Wang, H. Statistical Study of Free Magnetic Energy and Flare Productivity of Solar Active Regions. 2014, *Astrophys. J.* **2014**, *788*, 150 [CrossRef]
11. Chen, J.; Su, J.; Yin, Z.; Priya, T.G.; Zhang, H.; Liu, J.; Xu, H. and Yu, S. Recurrent Solar Jets Induced By a Satellite Spot and Moving Magnetic Features. *Astrophys. J.* **2015**, *815*, 71. [CrossRef]
12. Guo, J.; Wang, H.; Wang, J.; Zhu, X.; Dai, X.; Huang, X.; He, H.; Yan, Y. and Zhao, H. The Role of a Magnetic Topology Skeleton in a Solar Active Region. *Astrophys. J.* **2019**, *874*, 181. [CrossRef]
13. Ruan, G.; Chen, Y.; Wang, H. Gradual Magnetic Evolution of Sunspot Structure Furthermore, Filament-Corona Dynamics Associated With the X1.8 Flare in AR11283. *Astrophys. J.* **2015**, *812*, 120−127. [CrossRef]
14. Xu, H.; Su, J.; Chen, J.; Ruan, G.; Awasthi, A.K.; Zhang, H.; Zhang, M.; Ji, K.; Zhang, Y.; Liu, J. Multiwavelength Observation of a Failed Eruption from a Helical Kink-unstable Prominence. *Astrophys. J.* **2020**, *901*, 121. [CrossRef]
15. Yang, S.; Zhang, J.; Xiang, Y. Magnetic Reconnection between Small-scale Loops Observed with the New Vacuum Solar Telescope. *Astrophys. J. Lett.* **2015**, *798*, L11. [CrossRef]
16. Wyper, P.F.; Antiochos, S.K.; DeVore, C.R. A Universal Model For Solar Eruptions. *Nature* **2017**, *544*, 452−455. [CrossRef] [PubMed]
17. Zhang, Y.; Tan, B.L.; Tan, C.M.; Huang, J.; Yan, Y.H. Multi-Wavelength Observations of a Failed Filament Eruption and Associated Hovered Coronal Mass Ejection. *Universe* **2021**, *7*, 405. [CrossRef]
18. Moore, R.L.; Sterling, A.C.; Hudson, H.S.; Lemen, J.R. Onset of the Magnetic Explosion in Solar Flares and Coronal Mass Ejections. *Astrophys. J.* **2001**, *552*, 833. [CrossRef]
19. Antiochos, S.K.; DeVore, C.R.; Klimchuk, J.A. A Model for Solar Coronal Mass Ejections. *Astrophys. J.* **1999**, *510*, 485. [CrossRef]
20. Liu, L.J.; Wang, Y.M.; Zhou, Z.J.; Cui, J. The Source Locations of Major Flares and CMEs in Emerging Active Regions. *Astrophys. J.* **2021**, *909*, 142. [CrossRef]
21. Dai, J.; Li, Z.T.; Wang, Y.; Xu, Z.; Zhang, Y.J.; Li, L.P.; Zhang, Q.M.; Su, Y.N.; Ji, H.S. A Partial Filament Eruption in Three Steps Induced by External Magnetic Reconnection. *Astrophys. J.* **2022**, *929*, 85−96. [CrossRef]
22. Tian, L.R.; Alexander, D. Role of Sunspot and Sunspot-Group Rotation in Driving Sigmoidal Active Region Eruptions. *Sol. Phys.* **2006**, *233*, 29−43. [CrossRef]
23. Rust, D.M.; Kumar, A. Evidence for Helically Kinked Magnetic Flux Ropes in Solar Eruptions. *Astrophys. J. Lett.* **1996**, *464*, L199. [CrossRef]
24. Leka, K.D.; Fan, Y.; Barnes, G. On the Availability of Sufficient Twist in Solar Active Regions to Trigger the Kink Instability. *Astrophys. J.* **2005**, *626*, 1091 [CrossRef]
25. Régnier, S.; Amari, T.; Kersalé, E. 3D Coronal magnetic field from vector magnetograms: Non-constant-α force-free configuration of the active region NOAA 8151. *Astron. Astrophys.* **2002**, *392*, 1119−1127. [CrossRef]
26. Régnier, S.; Amari, T. 3D magnetic configuration of the H$_\alpha$ filament and X-ray sigmoid in NOAA AR 8151. *Astron. Astrophys.* **2004**, *425*, 345−352. [CrossRef]
27. Ruan, G.; Jejčič, S.; Schmieder, B.; Mein, P.; Mein, N.; Heinzel, P.; Gunár, S.; Chen, Y. Diagnostics of the Prominence Plasma from H$_\alpha$ and Mg II Spectral Observations. *Astrophys. J.* **2019**, *886*, 134−147. [CrossRef]
28. Jing, J.; Liu, C.; Lee, J.; Ji, H.; Liu, N.; Xu, Y.; Wang, H. Statistical Analysis of Torus and Kink Instabilities in Solar Eruptions. *Astrophys. J.* **2018**, *864*, 138. [CrossRef]
29. Wang, D.; Liu, R.; Wang, Y.M.; Liu, K.; Chen, J.; Liu, J.J.; Zhou, Z.J.; Zhang, M. Critical Height of the Torus Instability in Two-ribbon Solar Flares. *Astrophys. J. Lett.* **2017**, *843*, L9−L14. [CrossRef]
30. Pevtsov, A.A.; Canfield, R.C.; Metcalf, T.R. Latitudinal Variation of Helicity of Photospheric Magnetic Fields. *Astrophys. J. Lett.* **1995**, *440*, L109−L112. [CrossRef]

31. Abramenko, V.I.; Wang, T.; Yurchishin, V.B. Analysis of Electric Current Helicity in Active Regions on the Basis of Vector Magnetograms. *Sol. Phys.* **1996**, *168*, 75−89. [CrossRef]

32. Bao, S.; Zhang, H. Patterns of Current Helicity for Solar Cycle 22. *Astrophys. J. Lett.* **1998**, *496*, L43−L46. [CrossRef]

33. Zhang, H.; Moss, D.; Kleeorin, N.; Kuzanyan, K.; Rogachevskii, I.; Sokoloff, D.; Gao, Y.; Xu., H. Current Helicity of Active Regions as A Tracer of Large-Scale Solar Magnetic Helicity. *Astrophys. J.* **2012**, *751*, 47. [CrossRef]

34. Kutsenko, A.S.; Abramenko, V.I.; Pevtsov, A.A. Extended statistical analysis of emerging solar active regions. *Mon. Not. R. Astron. Soc.* **2019**, *484*, 4393−4400. [CrossRef]

35. Shen, Y.D.; Li, B.; Chen, P.F.; Zhou, X.P.; Liu, Y. Research Progress on Coronal Extreme Ultraviolet Waves. *Sci. Bull.* **2020**, *65*, 3909−3923. (In Chinese) [CrossRef]

36. Shen, Y.; Zhou, X.; Duan, Y.; Tang, Z.; Zhou, C.; Tan, S. Coronal Quasi-periodic Fast-mode Propagating Wave Trains. *Sol. Phys.* **2022**, *297*, 20. [CrossRef]

37. Scherrer, P.H.; Schou, J.; Bush, R.I.; Kosovichev, A.G.; Bogart, R.S.; Hoeksema, J.T.; Liu, Y.; Duvall, T.L., Jr.; Zhao, J.; Title, A.M.; et al. The Helioseismic and Magnetic Imager (HMI) Investigation for the Solar Dynamics Observatory (SDO). *Sol. Phys.* **2012**, *275*, 207−227. [CrossRef]

38. Sun, X.D. On the Coordinate System of Space-Weather HMI Active Region Patches (SHARPs): A Technical Note. *arXiv* **2013**, arXiv:1309.2392.

39. Bobra, M.G.; Sun, X.D.; Hoeksema, J.T.; Turmon, M.; Liu, Y.; Hayashi, K.; Barnes, G.; Leka, K.D. The Helioseismic and Magnetic Imager (HMI) Vector Magnetic Field Pipeline: SHARPs-Space-Weather HMI Active Region Patches. *Sol. Phys.* **2014**, *289*, 3549−3578. [CrossRef]

40. Liu, Y.; Hoeksema, J.T.; Bobra, M.; Hayashi, K.; Schuck, P.W.; Sun, X. Magnetic Helicity in Emerging Solar Active Regions. *Astrophys. J.* **2014**, *785*, 13. [CrossRef]

41. Liu, Y.; Zhao, J.; Schuck, P.W. Horizontal Flows in the Photosphere and Subphotosphere of Two Active Regions. *Sol. Phys.* **2013**, *287*, 279−291. [CrossRef]

42. Berger, M.A.; Field, G.B. The Topological Properties of Magnetic Helicity. *J. Fluid Mech.* **1984**, *147*, 133−148. [CrossRef]

43. Démoulin, P.; Berger, M.A. Magnetic Energy and Helicity Fluxes at the Photospheric Level. *Sol. Phys.* **2003**, *215*, 203−215. [CrossRef]

44. Yang, S.; Büchner, J.; Skála, J. and Zhang, H. Evolution of Relative Magnetic Helicity New Boundary Conditions for the Vector Potential. *Astron. Astrophys.* **2018**, *613*, A27. [CrossRef]

45. Berger, M.A.; Ruzmaikin, A. Rate of Helicity Production by Solar Rotation. *Geophys. Res.* **2000**, *105*, 10481−10489. [CrossRef]

46. Gao, Y. A Quantity Characterizing Variation of Observed Magnetic Twist in Solar Active Regions. *Res. Astron. Astrophys.* **2018**, *18*, 28. [CrossRef]

47. Zhang, H.; Sakurai, T.; Pevtsov, A.; Gao, Y.; Xu, H.; Sokoloff, D.; Kuzanyan, K. A New Dynamo Pattern Revealed by Solar Helical Magnetic Fields. *Mon. Not. R. Astron. Soc.* **2010**, *402*, L30−L33. [CrossRef]

48. Liu, J.H.; Liu, Y.; Zhang, Y.; Huang, J.; Zhang, H.Q. Helicity observations of active regions during the exchange period of Solar Cycle 24 and 25. *Mon. Not. R. Astron. Soc.* **2022**, *509*, 5298−5304. [CrossRef]

49. Liu, Y.; Hoeksema, J.T.; Sun, X. Test of The Hemispheric Rule of Magnetic Helicity in the Sun Using the Helioseismic and Furthermore, Magnetic Imager (HMI) Data. *Astrophys. J. Lett.* **2014**, *783*, L1−L6. [CrossRef]

50. Miao, Y.H.; Li, D.; Yuan, D.; Jiang, C.W.; Elmhamdi, A.; Zhao, M.Y.; Anfinogentov, S. Diagnosing a Solar Flaring Core with Bidirectional Quasi-periodic Fast Propagating Magnetoacoustic Waves. *Astrophys. J. Lett.* **2021**, *908*, L37. [CrossRef]

51. Hale, G.E. The Fields of Force in the Atmosphere of the Sun. *Nature* **1927**, *119*, 708. [CrossRef]

52. Zhang, Y.; Liu, J.H.; Zhang, H.Q. Relationship between Rotating Sunspots and Flares. *Sol. Phys.* **2008**, *247*, 39−52. [CrossRef]

53. LaBonte, B.J.; Georgoulis, M.K.; Rust, D.M. Survey of Magnetic Helicity Injection in Regions Producing X-class Flares. *Astrophys. J.* **2007**, *671*, 955. [CrossRef]

54. Liu, J.H.; Zhang, H.Q. The Magnetic Field, Horizontal Motion and Helicity in a Fast Emerging Flux Region Which Even-tually Forms a Delta Spot. *Sol. Phys.* **2006**, *234*, 21−40. [CrossRef]

55. Jiang, J.; Cameron, R. H.; Schüssler, M. Effects of the Scatter in Sunspot Group Tilt Angles on the Large-Scale Magnetic Field at the Solar Surface. *Astrophys. J.* **2014**, *791*, 5. [CrossRef]

56. Leka, K.D.; Canfield, R.C.; McClymont, A.N.; van Driel-Gesztelyi, L. Evidence for Current-carrying Emerging Flux. *Astrophys. J.* **1996**, *462*, 547. [CrossRef]

57. Wiegelmann, T. Optimization Code With Weighting Function for the Reconstruction of Coronal Magnetic Fields. *Sol. Phys.* **2004**, *219*, 87−108. [CrossRef]

58. Wiegelmann, T.; Inhester, B.; Sakurai, T. Preprocessing of Vector Magnetograph Data for a Nonlinear Force-Free Magnetic Field Reconstruction. *Sol. Phys.* **2006**, *233*, 215−232. [CrossRef]

59. Török, T.; Kliem, B. Confined and Ejective Eruptions of Kink-unstable Flux Ropes. *Astrophys. J.* **2005**, *630*, L97−L100. [CrossRef]

60. Zhang, Yin.; Tan, B.; Liu, J.; Yu, S.; Feng, S.; Chen, J.; Yan, Y. Multiwavelength Observations of the Formation and Eruption of a Complex Filament. *Astrophys. J.* **2021**, *910*, 40. [CrossRef]

61. Nindos, A.; Patsourakos, S.; Wiegelmann, T. On the Role of the Background Overlying Magnetic Field in Solar Eruptions. *Astrophys. J. Lett.* **2012**, *748*, L6. [CrossRef]
62. Liu, L.J.; Liu, J.J.; Chen, J.; Wang, Y.M.; Wang, G.Q.; Zhou, Z.J.; Cui, J. The configuration and failed eruption of a complex magnetic flux rope above a δ sunspot region. *Astron. Astrophys.* **2021**, *648*, A106. [CrossRef]